

L. Liao
A. K. Athienitis
L. Candanedo
K.-W. Park

Department of Building, Civil and Environmental
Engineering,
Concordia University,
1455 de Maisonneuve Blvd. West,
Montreal, QC, H3G 1M8

Y. Poissant
CANMET Energy Technology Centre—Varennes,
Natural Resources Canada,
1615 Lionel-Boulet Blvd.,
Varennes, QC, J3X 1S6

M. Collins
Department of Mechanical and Mechatronics
Engineering,
University of Waterloo,
200 University Avenue West,
Waterloo, Ontario, Canada N2L 3G1

Numerical and Experimental Study of Heat Transfer in a BIPV-Thermal System

This paper presents a computational fluid dynamics (CFD) study of a building-integrated photovoltaic thermal (BIPV/T) system, which generates both electricity and thermal energy. The heat transfer in the BIPV/T system cavity is studied with a two-dimensional CFD model. The realizable k - ϵ model is used to simulate the turbulent flow and convective heat transfer in the cavity, including buoyancy effect and long-wave radiation between boundary surfaces is also modeled. A particle image velocimetry (PIV) system is employed to study the fluid flow in the BIPV/T cavity and provide partial validation for the CFD model. Average and local convective heat transfer coefficients are generated with the CFD model using measured temperature profile as boundary condition. Cavity temperature profiles are calculated and compared to the experimental data for different conditions and good agreement is obtained. Correlations of convective heat transfer coefficients are generated for the cavity surfaces; these coefficients are necessary for the design and analysis of BIPV/T systems with lumped parameter models. Local heat transfer coefficients, such as those presented, are necessary for prediction of temperature distributions in BIPV panels. [DOI: 10.1115/1.2770750]

1 Introduction

Building-integrated photovoltaic (BIPV) systems are becoming increasingly popular in residential and commercial buildings because they serve as a functional part of the building envelope, thus decreasing structural installation costs while improving architectural integration. Such systems may serve not only as a renewable source of electricity, but also as a source of heat. The solar energy absorbed by the PV panel is partially converted to electricity and heat, and the rest is reflected. The generated heat may be partly dissipated to a cooling fluid to lower operating temperature for PV panels and thus to increase electrical conversion efficiency. In addition, by utilizing solar heat we improve the cost-effectiveness of the systems.

Various models and investigations on BIPV systems and double facades are reported in the literature. A 2D finite element model was employed in a CFD study by Moshfeg and Sandberg with idealized boundary conditions [1]. In 1996, a 2D laminar flow model was presented by Mootz and Bezan [2]. The BIPV model was further improved by introducing the radiation heat transfer in terms of the local surface temperature [3] while still mainly focusing on laminar flow. Zollner et al. [4] performed detailed experimental investigations and reported that the flow was turbulent mixed convection. They report some measurements of the low velocities, including different inlet sizes. In 2002, Mei et al. [5] presented a dynamic thermal model integrated to TRNSYS to study how the BIPV system can help to reduce the building load. However, none of the above studies used the real condition encountered in BIPV/T systems, which is a nonuniform temperature profile for the PV panel.

A full-scale test facility has been studied at Concordia University for nearly three years. A test room façade photo taken from outside is shown in Fig. 1. One- and two-dimensional models have been developed to study the thermal behavior in the air cavity [6,7]. However, these models, as well as similar models developed by other researchers (e.g., [8,9]) need accurate evaluation of convective heat transfer coefficients h_c for accurate thermal analysis and prediction of maximum PV panel temperature. Temperature differentials in the range of 10–20°C from the bottom to the top of a PV panel have been observed under cold sunny conditions [6]. Such differentials significantly affect the performance and long-term durability of photovoltaic panels. It is thus necessary to predict such differentials so as to select airflows that limit the maximum temperature of a PV panel to acceptable values and to provide useful input to configuration of PV arrays. This paper reports on a CFD study of the flow in the BIPV system, generation of the local convective heat transfer coefficients, and prediction of local PV temperatures. Air is drawn into the two side-by-side test sections with the aid of an exhaust fan located at the top in the room. Another part of this project considers integration with HVAC systems and control of the inlet damper and variable speed fan to achieve desired flow rates and supply temperatures.

2 Problem Description

The façade consists of a lower opaque section and an upper vision section. The vision section includes a motorized blind in the double façade cavity above the PV section, but this portion of the system is beyond the scope of this paper. The configuration considered in this paper is expected to be representative of practical application of the systems shown in Fig. 1. The cavity has width L equal to 0.092 m and height H equal to 1 m, as shown in Fig. 2. The outside air is drawn from the bottom inlet of the cavity, and the air intake temperature is measured. Based on experimental measurements, the flow has been established as two-dimensional and primarily turbulent due to the entrance effects,

Contributed by the Solar Energy Engineering Division of ASME for publication in the JOURNAL OF SOLAR ENERGY ENGINEERING. Manuscript received February 24, 2006; final manuscript received May 15, 2007. Review conducted by Moncef Krarti. Paper presented at the 2005 International Solar Energy Conference (ISEC2005), August 6–12, 2005, Orlando, FL.

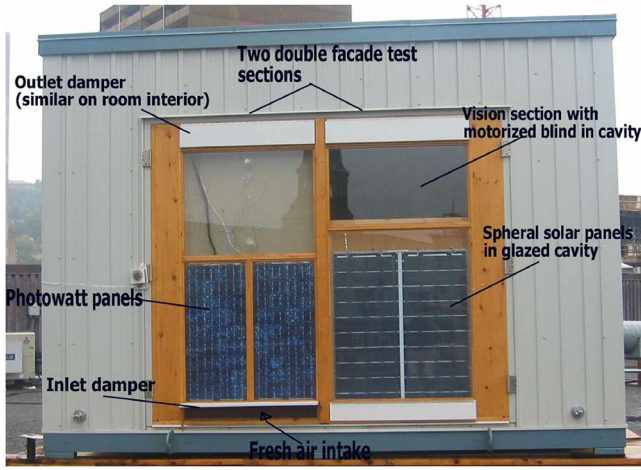


Fig. 1 Photograph of Concordia Building-integrated photovoltaic test facility

wind gusts, and cavity framing. The flow is assumed to be quasi-steady in the simulation model, and this is true if no significant thermal storage material is present in the façade. The PV panel is heated by the solar radiation and cooled by the airflow in the cavity so its surface temperature is a function of the height. The right-hand surface in Fig. 2 is assumed to be adiabatic (thermal insulation) but exchanges heat with the PV through long-wave radiation. A control volume-based finite difference method is used to simulate the flow in the cavity. The realizable k - ϵ model employed by FLUENT [10] is utilized with constant fluid properties except for the buoyancy term of the momentum equations, where the Boussinesq approximation is used to account for the density variation. The full buoyancy effect is also considered in the k - ϵ turbulent model. For the long-wave radiation heat transfer, view factors and radiosity are computed, and it is assumed that the surfaces are gray diffuse and the fluid is transparent to radiation. Since detailed analysis is desired near the boundaries, a finer grid is employed in those regions in addition to the enhanced wall treatment that is utilized for the k - ϵ turbulent model.

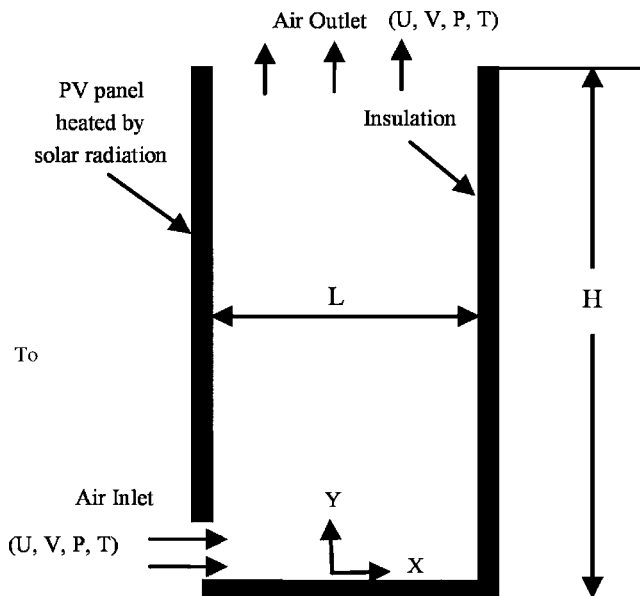


Fig. 2 Geometry of 2-D CFD model

3 Model Development

3.1 Governing Equations. Based on the above modeling assumptions, the governing equations for conservation of mass, conservation of momentum, conservation of energy, equation of the transport of turbulent kinetic energy, and equation of the turbulent energy dissipation are obtained as follows [10]: Continuity conservation equation

$$\frac{\partial}{\partial x}(\rho u) + \frac{\partial}{\partial y}(\rho v) = 0 \quad (1)$$

X-momentum conservation equation

$$\frac{\partial}{\partial x}(\rho uu) + \frac{\partial}{\partial y}(\rho uv) = -\frac{\partial P}{\partial x} + \frac{\partial}{\partial x}\left(\mu \frac{\partial u}{\partial x}\right) + \frac{\partial}{\partial y}\left(\mu \frac{\partial u}{\partial y}\right) \quad (2)$$

Y-momentum conservation equation

$$\begin{aligned} \frac{\partial}{\partial x}(\rho uv) + \frac{\partial}{\partial y}(\rho vv) = & -\frac{\partial P}{\partial y} - \rho g \beta (T - T_{\text{ref}}) + \frac{\partial}{\partial x}\left(\mu \frac{\partial v}{\partial x}\right) \\ & + \frac{\partial}{\partial y}\left(\mu \frac{\partial v}{\partial y}\right) \end{aligned} \quad (3)$$

Energy conservation equation

$$\frac{\partial}{\partial x}(\rho u T) + \frac{\partial}{\partial y}(\rho v T) = \frac{\partial}{\partial x}\left(\frac{K}{c_p} \frac{\partial T}{\partial x}\right) + \frac{\partial}{\partial y}\left(\frac{K}{c_p} \frac{\partial T}{\partial y}\right) \quad (4)$$

Equation of the transport of turbulent kinetic energy

$$\frac{\partial}{\partial t}(\rho k) + \frac{\partial}{\partial x_i}(\rho k u_i) = \frac{\partial}{\partial x_i}\left[\left(\mu + \frac{\mu_t}{\sigma_k}\right) \frac{\partial k}{\partial x_i}\right] + G_k + G_b - \rho \epsilon - Y_M + S_k \quad (5)$$

Equation of the turbulent energy dissipation

$$\begin{aligned} \frac{\partial}{\partial t}(\rho \epsilon) + \frac{\partial}{\partial x_j}(\rho \epsilon u_j) = & \frac{\partial}{\partial x_j}\left[\left(\mu + \frac{\mu_t}{\sigma_\epsilon}\right) \frac{\partial \epsilon}{\partial x_j}\right] + \rho C_{1\epsilon} S \epsilon - \rho C_{2\epsilon} \frac{\epsilon^2}{k + \sqrt{\nu \epsilon}} \\ & + C_{1\epsilon} \frac{\epsilon}{k} C_{3\epsilon} G_b + S_\epsilon \end{aligned} \quad (6)$$

where

$$C_1 = \max\left[0.43, \frac{\eta}{\eta + 5}\right], \quad \eta = S \frac{k}{\epsilon} \quad (7)$$

$$C_{1\epsilon} = 1.44, \quad C_{2\epsilon} = 1.9, \quad \sigma_k = 1.0, \quad \sigma_\epsilon = 1.2 \quad (8)$$

The surface-to-surface model is used to model the radiative heat transfer. The boundary surfaces are subdivided into many elements, and radiosity analysis is performed. Considering surface element k , we have net radiation from the surface element $q_{r,k}$, outgoing radiation from the element $q_{o,k}$, and incident radiation on the element $q_{i,k}$. These values can be calculated as follows: Net radiation from element k

$$q_{r,k} = q_{o,k} - q_{i,k} \quad (9)$$

Outgoing radiation from element k is equal to the emitted plus reflected radiation

$$q_{o,k} = \epsilon_k \sigma T_k^4 + \rho_k q_{i,k} \quad (10)$$

Incident radiation on element k is equal to the sum of the components from each surface

$$q_{i,k} = \sum_{j=1}^N F_{j,k} q_{o,j} \quad (11)$$

Equations (9)–(11) can be rearranged into matrix form as follows:

$$[A] \cdot [Q_o] = [S] \quad (12)$$

where

$$A_{i,j} = \delta_{i,j} - \rho_i F_{j,i} \quad (13)$$

$$S_k = \varepsilon_k \sigma T_k^4 \quad (14)$$

$$\delta_{i,j} = \begin{cases} 0, & \text{if } i \neq j \\ 1, & \text{if } i = j \end{cases} \quad (15)$$

3.2 Initial Values and Boundary Conditions. The air intake temperature is measured near the intake damper and is set as the inlet thermal boundary condition. Since the inlet velocity distribution is difficult to measure and sensitive to the final simulation results, the pressure difference condition is used for the inlet/outlet velocity boundary conditions. The pressure difference is precalculated based on the pressure loss calculation according to the respective average flow speed. The outlet condition is set to the outflow condition so that only the background temperature is needed for the long-wave radiation heat transfer calculation from the background. The left PV panel is the most active component in the whole system because it participates in several heat transfer exchanges: solar radiation at the outer surface, convection between the outer surface and the ambient air, background radiation between the outer surface and background, convection between the inner surface and flowing air inside the cavity, long-wave radiation between the inner surface and other surfaces inside the cavity, and possible conduction to the attached framing and other structures. Often, uniform temperature or uniform heat flux are assumed as boundary conditions, but for the short length used in this configuration, these idealized boundary conditions do not represent reality. In the present investigation, the measured PV temperature profile is used as boundary condition for the CFD simulations. As will be seen later, this profile is actually close to exponential.

The initial values of the flow parameters and boundary conditions have to be specified for the solution process. The initial values of temperature and velocities are set equal to the ambient conditions. The turbulence kinetic energy k and turbulent energy dissipation rate ε are set to 1. The boundary conditions are specified as follows:

1. Outlet boundary conditions: Pressure-outlet, $P=0$ (note that Boussinesq approximation is used and only the pressure difference matters)
2. Inlet boundary conditions: Pressure-inlet, $T=0^\circ\text{C}$, $P=P_{\text{in}}$ (range 0.3–2.0 Pa)
3. PV panel inner surface boundary conditions: $U=0$, $V=0$, $T(h)=T_{\text{pv}}(h)$ from experiment (measured temperature profile)
4. Other boundary conditions: $U=0$, $V=0$, adiabatic surface

3.3 Numerical Schemes and Mesh Generation. The governing Eqs. (1)–(8) with the given boundary conditions are solved by the control volume-based finite difference method using FLUENT 6.1. To facilitate numerical convergence, the pressure-velocity coupled problem is solved using SIMPLEC; momentum, energy, turbulence kinetic energy, and turbulence dissipation rate equations are solved using QUICK [10]. The underrelaxation factors for pressure, momentum, turbulence kinetic energy, and turbulence dissipation rate are set to 0.5, 0.7, 0.8 and 0.8, respectively. The convergence criteria are $<10^{-4}$ for all equations and 10^{-8} for the energy equation. A nonuniform grid (60×80) is utilized for boundary treatment as shown in Fig. 3; a large number of grid cells are placed at geometrically decreasing distances in the regions next to the walls where the largest gradients of velocity and temperature are expected. Since the flow is gradually heated by the PV panel and flow pattern develops slowly along the path, a y -direction grid interval of 5 cm was chosen. A coarser grid with

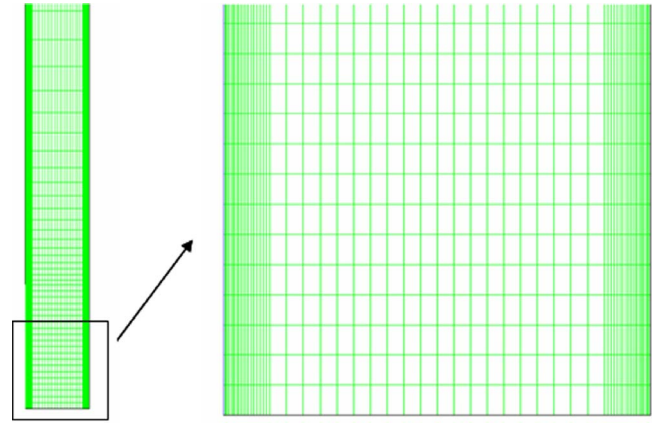


Fig. 3 Grid pattern of the boundary treatment

intervals of 10 cm at the main flow region was also tested, and no significant change was observed. The original mesh was refined twice also in x direction (80×80 , 120×80), and the same case was simulated with these meshes. The velocity, temperature, and convective heat transfer coefficient profiles were generated, and comparisons showed that they are in agreement within 2% with each other [11]. Therefore, further refinement of the mesh is not necessary.

4 Results and Analysis

The numerical results presented here were obtained using FLUENT 6.1 [10]. All the boundary surfaces have been assumed to be gray diffuse with emissivity equal to 0.9. The pressure difference between inlet and outlet is set to 0.5 Pa based on pressure drop calculation ($\Delta P = f(L/D)\rho(V^2/2)$, where f is friction factor, L is length, D is hydraulic diameter, and V is average velocity) for an average velocity of 0.5 m/s (measured). Note that iterations may be needed if CFD-generated average velocity is 10% or more different from this measured value. Different pressures are also considered to study the flow dynamics and thermal behavior under different flow rates. The Reynolds number for the present case is calculated to be between 10^3 and 10^4 , and the Rayleigh number is in the range of 10^7 – 10^8 . The Rayleigh number also depends on the boundary input of the PV panel temperatures. The temperature inputs for the PV panel are from experimental data for February 18, 2004 (see curve fit in Fig. 4).

4.1 Velocity and Temperature Profile. Figures 5(a) and 5(b) show the velocity profile at the top of the cavity from CFD simulations for different pressures and preliminary comparison to par-

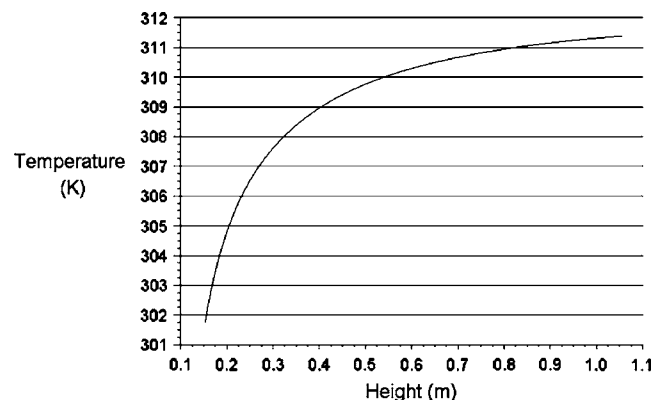


Fig. 4 Measured PV panel temperature used as boundary condition in CFD simulations

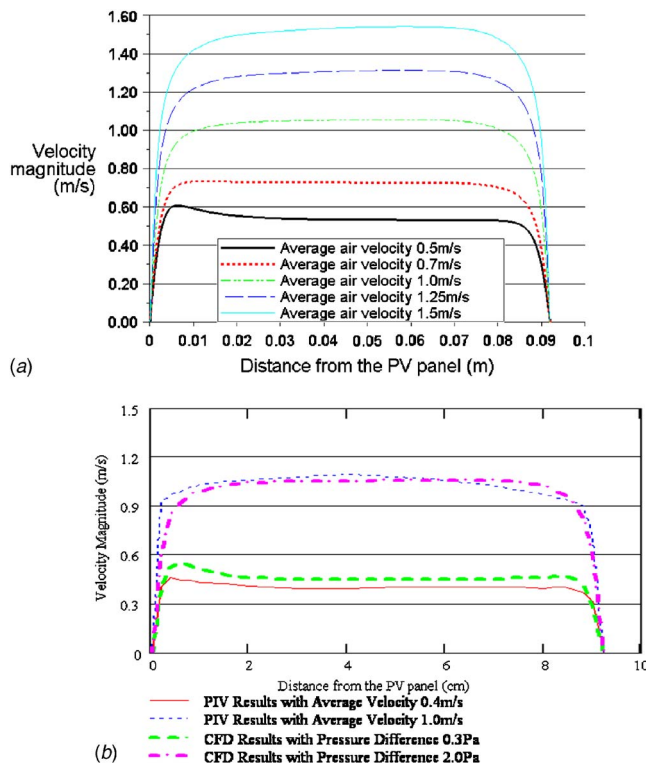


Fig. 5 (a). CFD model velocity profiles at the outlet of the PV section for different average air velocities. (b). Velocity profile from particle-image velocimetry (PIV) compared with CFD results for two flow rates.

particle image velocimetry (PIV) experimental data. In Fig. 5(b), average velocities of 0.4 m/s and 1 m/s (from PIV) correspond to a pressure drop of 0.3 Pa and 2 Pa, respectively. As can be seen from Fig. 5(b), the CFD and experimental results are generally close. As the pressure difference between the inlet and outlet increases, the average velocity increases gradually. For a low pressure difference of 0.3 Pa (average air velocity 0.4–0.5 m/s), we observe a buoyancy-induced peak in the velocity profile near the hot surface (PV panel). As the pressure difference between inlet and outlet is increased, we observe that forced convection dominates. It can be seen that the buoyancy-induced peak disappears and another small peak appears near the insulation side (average air velocity above 1.0 m/s). This velocity profile investigation can help understand that the flow is changing from natural convection to forced convection. At the average air speed 0.5 m/s, the pressure difference is ~ 0.5 Pa. This small pressure difference is not significant and is comparable to the pressure difference caused by the stack effect. Therefore, the buoyancy force near the PV panel is strong enough to influence the flow pattern. However, when the average air speed increases to 1.0 m/s, the pressure difference increases to ~ 2.0 Pa. This fan-induced pressure difference dominates the flow, and the stack effect becomes negligible. Another factor to consider is the inlet sharp turn, which will be improved by introducing turning vanes. Since the flow is still in the developing region and this sharp left turn will result in a higher speed at the right side of the air channel (simulation results are shown later in Fig. 8), a minor peak appears at the insulation side at average velocities above 1 m/s. This change is predicted from the simulations and is confirmed with the experimental measurements.

The comparison of the temperature profile at the top of the cavity from the modeling results and measurements from the experiment is shown in Fig. 6. The temperature falls sharply in the thermal boundary layer from 30°C to $\sim 4\text{--}6^\circ\text{C}$ and then remains flat in the inflow region until the thermal boundary layer near the

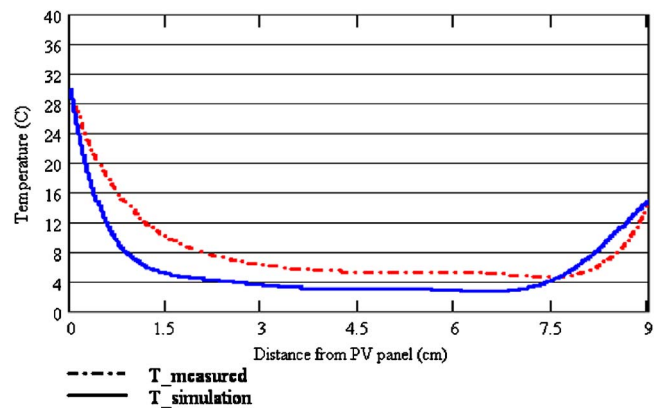


Fig. 6 Comparison of the outlet air temperature profile (at top of PV) from CFD model and experimental measurements

insulation, which is heated by the long-wave radiation from the PV panel. The insulation side is heated by long-wave radiation from PV panel (left) side. Since there is negligible heat flux through the insulation, the convection heat transfer should equal the net radiation heat transfer. Thus, the convection heat transfer from the insulation is not only determined by the flow dynamics but also influenced by the PV and insulation surface radiative properties. Since the flow is in the developing region, the local wind effect also affects the heat transfer. Further investigation with combination of wind effect will be performed in a following study. The difference between the CFD and experimental measurements may be attributed to deviations from the assumed boundary conditions, especially those at the inlet where there is 90 deg turn, framing, and some wind effects.

4.2 Convective Heat Transfer Coefficient Profile. In this paper, the local convective heat transfer coefficient h_c is defined as the local heat flux per unit area divided by the difference of local surface temperature and reference temperature ($h_c = q'' / (T - T_{\text{ref}})$). To be able to integrate with lumped parameter models such as [6], reference temperature is defined as the air intake temperature. Figure 7 shows the CFD-calculated convective heat transfer coefficient profiles for the two main cavity surfaces: the PV surface and insulation. Typical winter conditions in Montreal are simulated. The boundary conditions are set according to the experimental data. The intake air temperature is set to 0°C and average air speed 0.5 m/s. The PV temperature is specified based on a curve fit of the measurements, as shown in Fig. 4. As expected, at the leading edge, which is just after the inlet, the convective heat

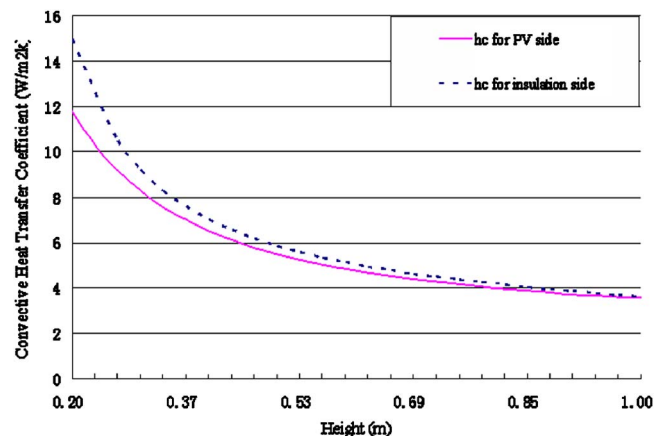


Fig. 7 Convective heat transfer coefficient profile at PV panel interior surface and at insulation

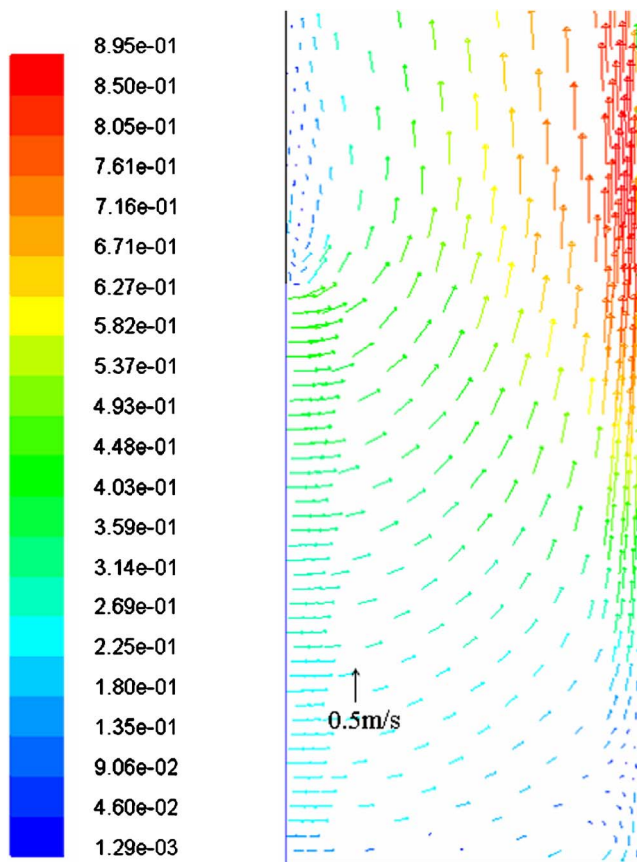


Fig. 8 Modeling (CFD) results around inlet flow region

transfer coefficient is quite high and that is also why the PV boundary temperature profile increases exponentially as expected (see Fig. 4). In addition, although the buoyancy effect increases the heat flux near the PV panel, the convective heat transfer coefficient at the insulation side is still higher. First, since the inlet is at the bottom left side, the air enters, then turns and has a significant velocity component toward the insulation surface. This can be seen from the velocity domain simulation of 2D CFD model, as shown in Fig. 8. The velocity near the insulation is faster than near the PV panel side; thus, the convective heat transfer is higher near this surface. Second, the insulation surface is further heated by the long-wave radiation and, because there is no heat flux through the insulation, the insulation heats up and transfers the energy by convection to the air. This has also been observed in a PIV investigation reported in more detail in a related paper by Liao [11].

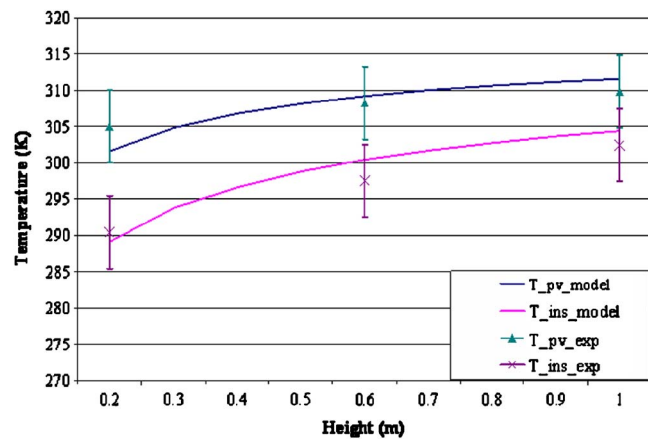


Fig. 9 Comparison of the predicted PV and insulation temperature profile with experimental data for March 29, 2004

4.3 Average and Local PV Temperature. The average convective heat transfer coefficient is calculated to be $5.8 \text{ W/m}^2 \text{ K}$ for the PV panel and $8.6 \text{ W/m}^2 \text{ K}$ for the insulation (average of the two is $7.1 \text{ W/m}^2 \text{ K}$). The heat transfer coefficients are validated for the velocity range from 0.3 m/s to 0.6 m/s and ambient temperatures from -10°C to 10°C . In this region, the flow is mainly natural convection, and convective heat transfer coefficients remain relatively stable. The radiation heat transfer coefficient is $\sim 4.8 \text{ W/m}^2 \text{ K}$. These values are substituted into a modified 1D model [6,7] to predict the PV and insulation temperatures. The 1D model with two different convective heat transfer coefficients [7] predicted by the two-dimensional CFD model is used to calculate the surface temperature for PV panel and insulation. Table 1 shows the comparison of predicted temperatures and experimental data for several days in Montreal. The predicted temperatures match the experimental results within 2°C . (Note the 0.05 m/s test on Feb. 11, 2005 is a one-day closed-channel test and h values are from experimental measurements.)

The computed convective heat transfer coefficient profiles were utilized in the two-dimensional model by Charron and Athienitis [6], and local PV cell temperatures were calculated as shown in Fig. 9. The ambient conditions on March 29, 2004 were used in the 2D model, and the calculated PV and insulation temperature profiles are compared to the experimental data on that day. The PV panel and insulation were divided into nine control volumes and solved with the finite volume method (upwind scheme). The model results shown match the experimental data within 3°C .

4.4 Convective Heat Transfer Coefficient Correlation. The computed convective heat transfer coefficients were modeled with a correlation as a function of average air velocity and position

Table 1 Comparison of experimental and predicted temperatures under quasi-steady state conditions

Date (2004)	Experimental data					Input heat transfer coefficients				Calculated results	
	Incident solar radiation (W/m^2)	Average velocity (m/s)	T_o ($^\circ \text{C}$)	T_{pv} ($^\circ \text{C}$)	T_{in} ($^\circ \text{C}$)	h_o ($\text{W/m}^2 \text{ K}$)	h_{pv} ($\text{W/m}^2 \text{ K}$)	h_{in} ($\text{W/m}^2 \text{ K}$)	h_r ($\text{W/m}^2 \text{ K}$)	T_{pv} model ($^\circ \text{C}$)	T_{in} model ($^\circ \text{C}$)
Feb. 8	1096	0.60	-14.1	21.0	1.7	15	5.8	8.6	4.8	21	4
Feb. 11	1031	0.05	-6.7	34.0	25.4	15	5.0	5.0	4.8	34	28
Feb. 18	858	0.30	-4.0	25.8	10.0	15	5.8	8.6	4.8	24	12
Mar. 10	768	0.30	3.4	35.7	19.1	10	5.8	8.6	4.8	36	21
Mar. 22	944	0.40	-11.4	21.7	6.1	14	5.8	8.6	4.8	21	8
Mar. 29	714	0.40	9.7	34.5	23.6	14	5.8	8.6	4.8	34	24
Mar. 30	712	0.30	10.8	37.2	25.9	13	5.8	8.6	4.8	37	25

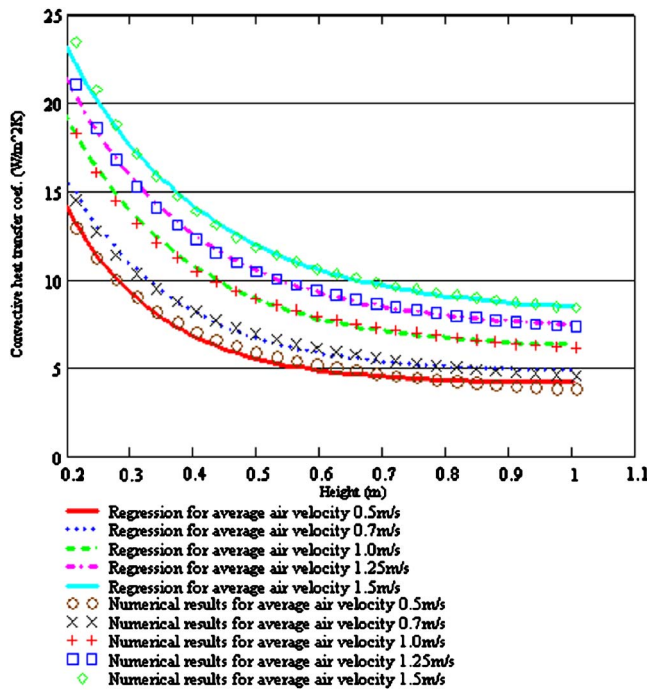


Fig. 10 Regression of the numerical results of convective heat transfer coefficients at PV panel side

height. This correlation can be used to calculate the local convective heat transfer coefficient at any position and at any average air velocity for single storey applications of BIPV systems.

From the shape of the profile plotted in Fig. 7, we can observe that the convective heat transfer coefficients points fall into the exponential correlation with channel height. Thus, the typical exponential correlation ($h_c = ae^{by} + c$) is used here for regression. Since the coefficients of this exponential correlation are also a function of average air speed, a double-regression has to be made to generate the correct function for both the height and average air speed.

The regressed correlation for h_c at the PV panel side was obtained as follows in ($W/m^2 K$):

$$h_c = 36.3e^{(2.042\bar{V}-7.375)y} + 3.987\bar{V} + 2.127 \quad (16)$$

and the regressed correlation for h_c at the insulation side is given by ($W/m^2 K$):

$$h_c = (184.946\bar{V} - 32.715)e^{(-1.144\bar{V}-6.439)y} + 6.927\bar{V} + 1.025 \quad (17)$$

where y is the channel height and \bar{V} is the average air speed in the y direction.

The numerical results and regression profile of the convective heat transfer coefficients are plotted in Figs. 10 and 11. As can be seen there is a good fit of the regression curves to the numerical results (they fit the data points within $\pm 3\%$).

For applications of the present results in simple lumped parameter models, the average convective heat transfer coefficients and radiative heat transfer coefficients are summarized in Table 2 and the correlation is generated and plotted in Fig. 12. From the correlation graph, we may observe that the convective heat transfer coefficients are increasing significantly as the average flow speed increases. In addition, the convective heat transfer coefficient at

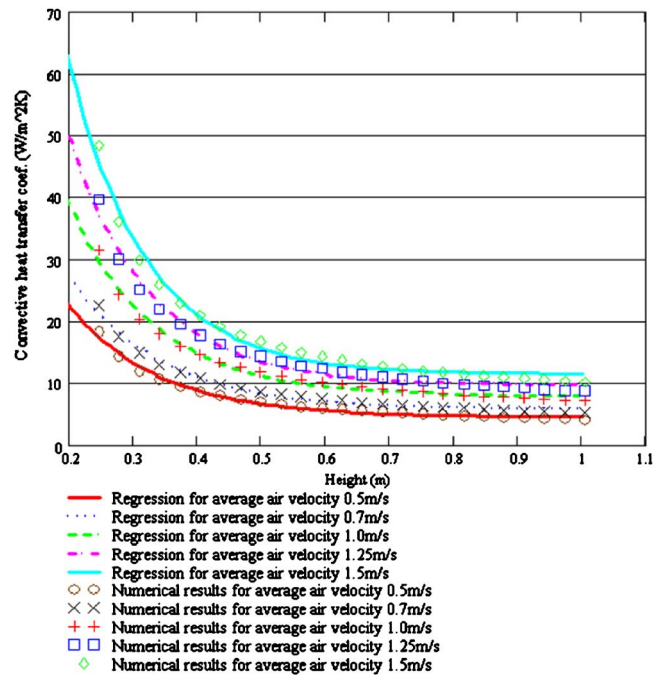


Fig. 11 Regression of the numerical results of convective heat transfer coefficients at insulation side

the insulation side has a higher start value. This is mainly because the flow is coming from the left bottom (PV side) of the cavity and forms a blowing region at the leading edge of the insulation side.

To generalize this convective heat transfer problem in the air-flow channel, nondimensional characteristic numbers are calculated. For this 2D fluid flow problem, the cavity gap width is the best value to be used as the characteristic length, and thus the Reynolds number can represent the airflow dynamics well and will not change along the channel height. The local Nusselt number (Nu_H) may be used to represent the dimensionless convective heat transfer coefficients along the channel height. We have the following definitions for local Nusselt number and for Reynolds number, respectively:

$$Nu_H = \frac{h_c(\bar{V}, y)L}{K_{air}} \quad (18)$$

$$Re = \frac{\rho \bar{V} L}{\mu} \quad (19)$$

where h_c is the local convective heat transfer coefficient and H is the dimensionless channel height, $H = y/L$

The correlation equation obtained for the local Nu_H at the PV panel side is given by

$$Nu_H = (0.011 Re + 62.856)e^{-0.475H} + (2.766 \times 10^{-3})Re + 5.58 \quad (20)$$

The correlation equation at the insulation side is as follows:

$$Nu_H = (0.109 Re - 124.344)e^{[-1.635 \times 10^{-5} Re - 0.593]H} + (4.098 \times 10^{-3})Re + 3.896 \quad (21)$$

The regression Eqs. (13) and (14) fit the data points within $\pm 3\%$. (See also, Figs. 13 and 14.) The decreasing trend of the Nusselt number along the channel height observed and high Nusselt number can be observed near the leading edge as expected. Values from the literature are comparatively lower than this correlation (e.g., [3,9]). Brinkworth [3] used the Nusselt number de-

Table 2 Summary of average heat transfer coefficients in the BIPV airflow cavity as a function of average air velocity

Average air velocity (m/s)	Convective heat transfer coefficient for PV panel (W/m ² K)	Convective heat transfer coefficient for insulation (W/m ² K)	Radiative heat transfer coefficient (W/m ² K)
0.5	5.8	8.6	4.8
0.7	6.9	10.3	4.8
1.0	8.8	13.6	4.8
1.25	10.2	15.8	4.7
1.5	11.5	17.9	4.7

veloped from thermally developed channel flow with a fully developed velocity profile from the beginning. Therefore, there is less heat flux at the leading edge and the Nusselt numbers are lower than the correlation given in this paper at the inlet region. In his paper, the Nusselt numbers at the heated surface side start from 55 at the inlet region and fall to 28 at the height ratio (H/D) 100 for $Re_D=10,000$. However, we can see that our correlation at the height ratio 11 with a Nusselt number 34 is near the value given by Brinkworth [3], which is 32. Since the air dynamics are sensitive, especially at the inlet region and developing region, the calculated convective heat transfer coefficients or Nusselt numbers may be easily influenced by the boundary settings and ambient conditions. In addition, it should be noted that the BIPV/T system considered is only ~ 1 m high and the leading-edge effects are strong. Also, the flow becomes turbulent early because of the turn at the inlet region and buoyancy effect at the PV surface. PIV measurements showed 10–15% turbulence intensity for configuration 1 (photowatt side) and 10–20% at different positions for configuration 2 (spherical solar side). However, from the trend of the correlation we can easily predict that when the flow is becoming fully developed at larger heights the correlation will correlate with the literature more closely. It should be noted, however, that for one-story applications of BIPV-thermal systems, the correlations presented here will be particularly useful, provided the long-wave radiation heat transfer is also appropriately modeled.

5 Conclusions

This paper presented a CFD study of heat transfer and fluid flow in a building-integrated photovoltaic-thermal system intended for single story applications. Although the main case of interest in this paper is forced convection with fan-induced airflow, at low pressure differentials there is a buoyancy-induced velocity peak near the PV surface. The heat transfer coefficients were predicted for the two cavity surfaces, and the convective

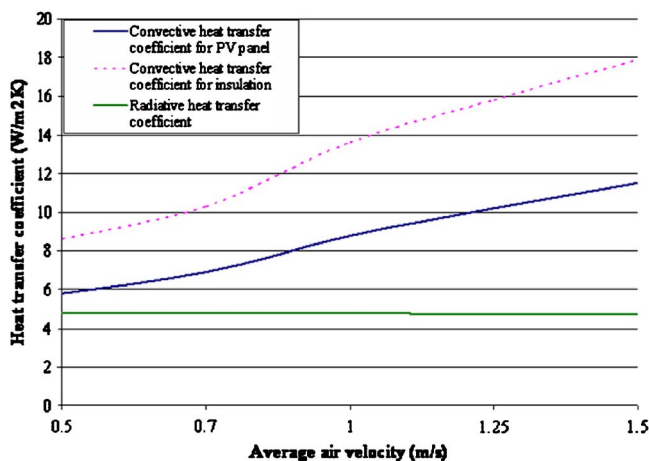


Fig. 12 Correlation of heat transfer coefficients as a function of average air velocities

coefficient was determined through a combination of CFD simulations and experimental measurements that provided boundary conditions; the convective coefficients were generally higher than expected by other correlations [6,7] due to leading-edge effects and the turbulent nature of the flow. Experimental measurements of the velocity profiles in the BIPV system cavity using a particle image velocimetry system were in good agreement with CFD model predictions. The heat transfer coefficients calculated can be utilized in simpler models to facilitate the design of BIPV/T systems. Correlations have been developed for the convective heat transfer coefficients and as a function of commonly used dimensionless numbers.

Acknowledgment

Financial support for this collaborative research project was provided through an NSERC strategic grant and by Natural Resources Canada (NRCAN) through the Innovative Research Initiative and the Technology and Innovation Program as part of the

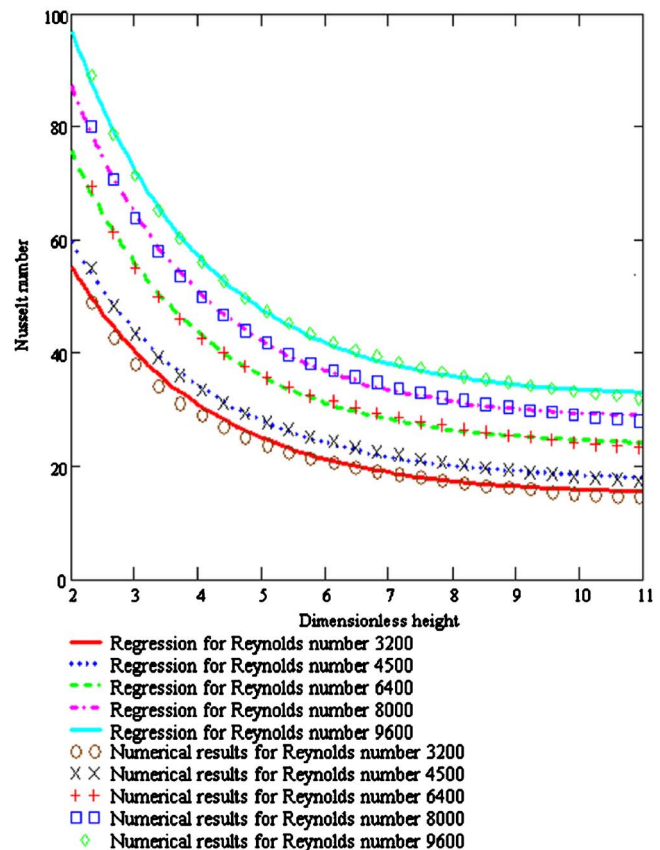


Fig. 13 Correlation (regression) profile of Nu numbers at the PV panel side

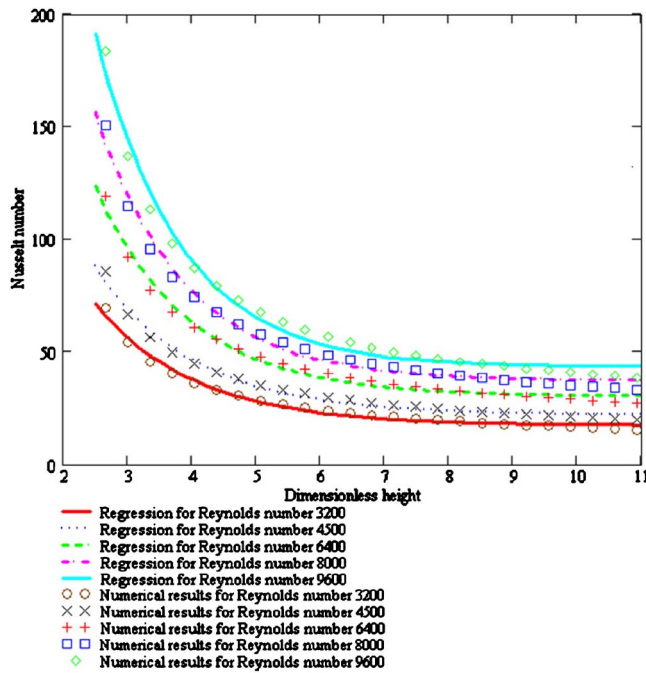


Fig. 14 Correlation (regression) profile of Nu numbers at insulation side

Climate Change Plan for Canada. ATS (Spheral Solar Power Inc.) and CANMET (CETC Varennes) also provided extensive support for this project.

Nomenclature

BIPV/T	= building integrated photovoltaic-thermal
C_p	= specific heat capacity of air
$F_{i,j}$	= view factor from surface i to surface j
G	= incident solar radiation
G_b	= generation of turbulent kinetic energy due to buoyancy
G_k	= generation of turbulent kinetic energy due to the mean velocity gradients
H	= height of cavity in BIPV system
h_c	= convective heat transfer coefficient in cavity
h_o	= exterior heat transfer coefficient
h_r	= radiative heat transfer coefficient
K	= thermal conductivity of air
k	= turbulent kinetic energy
PV	= photovoltaic

$q_{r,k}$	= net radiative heat transfer from surface element k
$q_{o,k}$	= outgoing radiative heat transfer from the k element
$q_{i,k}$	= incident radiation on element k
S_k	= user-defined source term for k
S_ε	= user-defined source term for ε
T	= air temperature in the cavity
T_{ref}	= reference temperature of air flow
T_{in}	= insulation temperature (facing cavity in BIPV system)
U	= air velocity in the x direction
V	= air velocity in the y direction
W	= width of cavity
x	= horizontal direction in the airflow cavity
y	= vertical direction in the airflow cavity
Y_M	= contribution of the fluctuating dilatation in compressible turbulence to the overall dissipation rate
ε	= turbulent energy dissipation rate
ρ	= air density
σ_k	= turbulent Prandtl number for k
σ_ε	= turbulent Prandtl number for ε

References

- [1] Moshfegh, B., and Sandberg, M., 1996, "Investigating of Fluid Flow and Heat Transfer in a Vertical Channel Heated From One Side by PV Elements Part I—Numerical Study," World Renewable Energy Congress, pp. 248–253.
- [2] Mootz, F., and Bezan, J. J., 1996, "Numerical Study of a Ventilated Façade Panel," Sol. Energy, **57**(1), pp. 29–36.
- [3] Brinkworth, B. J., 2002, "Coupling of Convective and Radiative Heat Transfer in PV Cooling Ducts," ASME J. Sol. Energy Eng., **124**, pp. 250–255.
- [4] Zollner, A., Winter, E. R. F., and Viskanta, R., 2002, "Experimental Studies of Combined Heat Transfer in Turbulent Mixed Convection Fluid Flows in Double-Skin-Façades," Int. J. Heat Mass Transfer, **45**, pp. 4401–4408.
- [5] Mei, L., Infield, D., Eicker, U., and Fux, V., 2003, "Thermal Modelling of a Building With an Integrated Ventilated PV Façade," Energy Build., **35**(6), pp. 605–617.
- [6] Charron, R., and Athienitis, A. K., 2006, "A Two-Dimensional Model of a Double-Façade With Integrated Photovoltaic Panels," ASME J. Sol. Energy Eng., **128**, pp. 160–167.
- [7] Charron, R., and Athienitis, A. K., 2006, "Optimization of the Performance of Double-Façades With Integrated Photovoltaic Panels and Motorized Blinds," Sol. Energy, **80**(5), pp. 482–491.
- [8] Bazilian, M., Leenders, F., Van Der Ree, B. G. C., and Prasad, D., 2001, "Photovoltaic Cogeneration in the Built Environment," Sol. Energy, **71**, pp. 57–69.
- [9] Sparrow, E. M., Garcia, A., and Chuck, W., 1986, "Numerical and Experimental Turbulent Heat Transfer Results for a One-sided Heated Rectangular Duct," Numer. Heat Transfer, **9**, pp. 301–322.
- [10] FLUENT, 6, 2002, User's Guide, ANSYS Inc., Canonsburg, PA.
- [11] Liao, L., 2005, "Numerical and Experimental Investigation of Building-Integrated Photovoltaic-Thermal Systems," M.A.Sc thesis, Dept. of Building, Civil and Environmental Engineering, Concordia University, Montreal, Quebec.